applied sciences

MDPI

Article

Analysis of Building Platform Inhomogeneities in PBF-LB/M Process on Alloy 718

Niccolò Baldi [1,2], Lokesh Chandrabalan [2], Marco Manetti [2], Alessandro Giorgetti [3,*], Gabriele Arcidiacono [1], Paolo Citti [1] and Marco Palladino [2]

[1] Department of Engineering Science, Guglielmo Marconi University, 00193 Rome, Italy; niccolo.baldi2@bakerhughes.com (N.B.); g.arcidiacono@unimarconi.it (G.A.); p.citti@unimarconi.it (P.C.)
[2] Baker Hughes—Nuovo Pignone, Via Felice Matteucci 2, 50127 Florence, Italy; lokesh.chandrabalan@bakerhughes.com (L.C.); marco.manetti@bakerhughes.com (M.M.); marco.palladino@bakerhughes.com (M.P.)
[3] Department of Industrial, Electronic and Mechanical Engineering, Roma Tre University, 00146 Rome, Italy
* Correspondence: alessandro.giorgetti@uniroma3.it

Abstract: Additive Manufacturing (AM) processes, particularly PBF-LB/M, are considered advantageous due to their flexibility, which allows process engineers to design and fabricate intricate structures both in the prototyping and component manufacturing phases. It is well known that the behavior of the process directly impacts the quality of the materials and thereby induces inhomogeneities on the powder bed on the building platform. Several parameters can be tuned to keep the process under control, getting rid of process uncertainty and distinguishing aspects of a specific machine model. Such behavior requires an extended analysis of the powder bed inhomogeneities and the definition of limits in the printing process. In this work, carried out on Alloy 718 specimens printed using an EOS M290 machine, the inhomogeneities of the melt pool stability, density, and material properties were investigated based on three main factors: the amount of area melted or fused, the gas flow speed setpoint, and the location on the building platform. The test results for Track Stability, melt-pool shape, and porosity analysis show that criticality occurs when more than 50% of the building platform is exposed. This can be partly fixed by raising the differential pressure value.

Keywords: additive manufacturing; PBF-LB/M; Alloy 718; building platform; melt-pool shape; single track analysis

Academic Editor: Thang Quyet Tran

Received: 3 February 2025
Revised: 28 March 2025
Accepted: 2 April 2025
Published: 7 April 2025

Citation: Baldi, N.; Chandrabalan, L.; Manetti, M.; Giorgetti, A.; Arcidiacono, G.; Citti, P.; Palladino, M. Analysis of Building Platform Inhomogeneities in PBF-LB/M Process on Alloy 718. *Appl. Sci.* **2025**, *15*, 4042. https://doi.org/10.3390/app15074042

1. Introduction

Additive manufacturing (AM) is the most advanced and notable metal-processing technology specializing in the precise fabrication of arbitrarily shaped structures [1–8]. Recently, Powder Bed Fusion-Laser Beam/Metal (PBF-LB/M) has captured global attention as a cutting-edge AM technology that has matured over an extended period of research and industrial development in the past decade. PBF-LB/M compared to other metal AM techniques, enables high accuracy and lower distortions of the final part, due to low heat generation during the melting process [9,10]. This additive manufacturing technology facilitates the production of various metal alloys, particularly nickel-based superalloys, which are challenging to manipulate using conventional subtractive methods due to their hardness and poor thermal conductivity.

The maturity of this AM technology is highly evident with the wide uptake in the production of commercial products, especially to create high-value products that cannot

be technically feasible using conventional manufacturing methods. It has been shown that the PBF-LB/AM process can change the shape of metal parts, their crystallographic structure [11–13], and their related mechanical and chemical characteristics [14–16] by optimizing various process parameters. The most influential factors among the various process parameters that impact the PBF-LB/M process, either directly or indirectly, include Laser Power, Scanning Speed, Hatch Distance, and Layer Thickness [17–22]. In particular, the formation of the Melt Pool is influenced by Laser Power and Scanning Speed. Therefore, it is crucial to identify the appropriate values for these parameters to prevent phenomena such as Keyhole [23–25], Lack of Fusion, and Balling [26–28], and to ensure that the melting regime of the powder operates in conduction mode [29–31]. During the building process, inert gases such as argon or nitrogen are generally used as shielding gases to prevent metal from oxidation and eliminate byproducts such as spatters and fumes produced in the interaction area of the laser and metal powders, which could potentially impact the quality and the microstructure of the fabricated products [2,32–35]. The fundamental variables influencing the quality and characteristics of manufactured products encompass the physical properties and flow direction of the gas. It should be mentioned that the gas flow in the PBF-LB/M process chamber is generally unidirectional, meaning that the outlet of the gas is located on the other side of the building platform from the inlet. In order to guarantee the quality of the building process, different laser scanning strategies have been proposed and implemented depending on the objectives, such as reducing residual stress, improving shape accuracy [35], and obtaining optimal microstructures [36].

On the other hand, using a low-density, high-thermal-conductivity gas such as helium in the process chamber can improve factors such as mechanical properties [37], the melt pool depth [38], and build speed [39], and suppress byproducts [37]. However, it must be noted that if the shielding inert gas flow is not well designed to assure the quality of the component, the laser windows and lenses could be contaminated with debris from the byproducts. This, in turn, leads to the attenuation and defocusing of the laser beam, generates instability in the building process, and promotes the formation of Lack of Fusion porosity in the material. In the work conducted by Reijonen et al. [40], various levels of shielding gas flow speed were investigated to study variations in the material in terms of porosity and single-track. However, it is also important to understand the effects of shielding gas in terms of varying the exposed area to replicate the actual building conditions. The aim of this work is to investigate, for a specific and commercial PBF-LB/M machine model, the inhomogeneities of material printability depending on the building platform location, the area exposed, and the gas flow setpoint value (set on the machine as “differential pressure”). The material selected for the study is Alloy 718, which is widely used for high-temperature applications especially in aerospace and energy sectors. Consequently, this work aims to achieve a high production rate by studying the methods that enable the extensive use of the entire building platform.

In order to characterize and quantify the building platform inhomogeneities by varying the amount of area printed on the building platform, gas flow speed setpoint, and building platform location, a Single-Track [41–46] and Porosity analysis, evaluating the track’s stability level, Melt Pool shape, and material density and defects distribution, was carried out.

2. Materials and Methods

All the specimens manufactured and analyzed in this experimental campaign were produced in Alloy 718, one of the most widely used nickel-based alloys in the PBF-LB/M process [47]. The chemical composition, mechanical, and physical properties of Alloy 718 are reported in Tables 1 and 2 [20,48].

Table 1. Chemical composition of Alloy 718 [20].

Element	% Weight
Ni	55.37
Cr	18.37
Fe	17.80
Nb + Ta	5.34
Nb	5.33
C	0.040
Mn	0.08
Si	0.08
P	<0.015
S	0.002
Co	0.23
Mo	3.04
Ti	0.98
Al	0.5
B	0.004
Ta	0.005
Cu	0.04
Ca	<0.01
Mg	<0.01
Pb	0.0001
Bi	0.0001
Se	<0.001

Table 2. Main mechanical and physical properties of Alloy 718 processed through PBF-LB/M process [20].

Elastic Modulus (Gpa)	Density (kg/m^3)	Thermal Conductivity (W/mK)	Yield Strength (MPa)	Tensile Stress (MPa)	Strain (%)
206	8470	11.2	1100	1310	23.3

The layer thickness used to slice and build the specimens was 40 microns. The particle size distribution (PSD) of the powder, achieved via a gas atomization process, was evaluated in the range between 20 and 63 microns.

An EOS Eosint M290 (EOS GmbH, Krailling, Germany) with a single ytterbium fiber laser that had a beam wavelength of 1070 nm, a minimum laser beam spot size of 80 µm, and a maximum laser power of 400 W was the apparatus utilized for all of the tests. The building platform, with dimensions of 250 mm × 250 mm × 30 mm, was made with C40 steel and maintains a stable temperature of 80 °C throughout the printing process. Continuous pumping of argon gas was utilized within the building chamber to ensure that the oxygen content remained below 100 ppm.

The aim of this work, as previously mentioned and described in the Introduction section, is to investigate the inhomogeneities in terms of material printability on the building platform as a function of the area exposed and, in turn, the creation of spatter and by-products. According to previous studies carried out on EOS Eosint M-290 machines concerning the gas flow system architecture, the lower part, closed to the outlet nozzle, is identified as the most critical region during the printing phase [49]. All the tested specimens were printed with the process parameters set used in a previous paper [50] for 40 microns of layer thickness (Laser Power: 270 W; Scanning Speed: 960 mm/s; Hatch Distance: 0.11 mm) and with a constant recoater speed. The study focuses on the lower part of the building

platform because a previous study [49] did not observe evidence of material printability degradation along the vertical direction.

As illustrated in Figure 1, a customized layout of Job is defined in order to accurately explore this phenomenon. In particular, to have a clear understanding of the effect of the exposed area on printability inhomogeneities on the building platform, six levels of this parameter are investigated, as mentioned in Table 3, starting from a condition of almost total exposure of the building platform of EOS M-290.

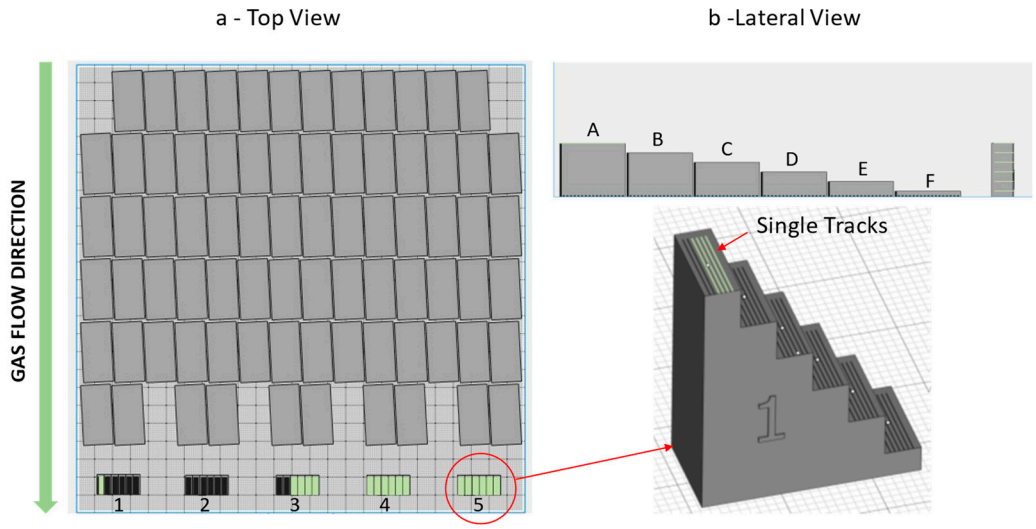

Figure 1. Job layout and specimen design: (**a**) Top view, (**b**) Lateral view. The dimensions of each grid square are 10 mm × 10 mm.

Table 3. Investigated levels of area exposed.

Section	Exposed Area (% in Terms of Building Platform Overall Area)
A	70
B	59
C	48
D	37
E	26
F	15

The powder bed inhomogeneities are measured and quantified in terms of the track's stability, Melt Pool, and Porosity analysis using a "ladder" shaped specimen. We specifically evaluate the presence of porosity for its ability to change the microstructure and subsequently deteriorate the mechanical properties of the materials [51]. Each specimen is provided with six single tracks on its top surface and placed in five positions in the lower part of the building platform, as shown in Figure 1. The dimensions of the specimen and Single Tracks are reported in Figure 2.

In particular, the Single Track's stability level for each specimen is evaluated through SEM analysis of the 36 (six Single Tracks for each of the six levels) printed Single Tracks (Figure 2) with a magnification of 40× on the microscope (TESCAN MIRA 4, Tescan, Brno, Czech Republic). The algorithm and criteria adopted to evaluate the level of stability of Single Tracks is based on the calculations of the number of interruptions along the length of the track as fully described in [20].

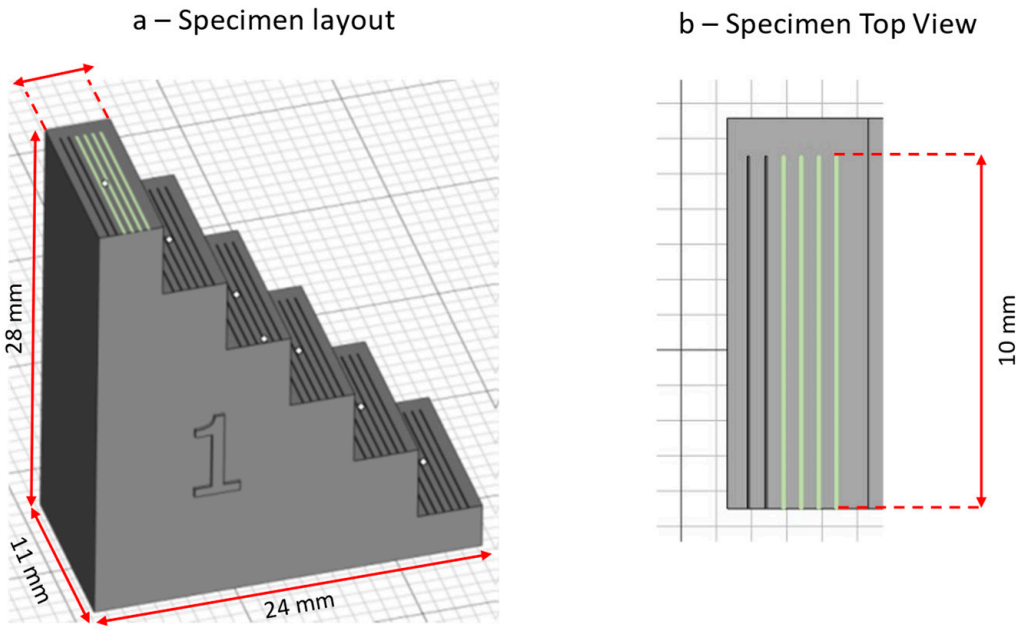

Figure 2. (**a**) Specimen layout and dimensions; (**b**) Single Track dimensions on the top surface of the specimen.

Once the Single Track analysis is completed, the specimens need to be prepared for micrographic analysis to evaluate Porosity levels and the quality of the Melt Pool. Next, we cut the specimens along the red-highlighted face in Figure 2, maintaining a distance of 5 mm from the edge. This is primarily to avoid edge effects and to analyze the Melt Pool in a steady-state condition. The specimens are then embedded in conductive resin and finally polished.

To accurately evaluate the six fields on the sample, we perform porosity analysis using an optical microscope with a magnification of 50×.

In order to highlight the Melt Pool boundaries, the specimens are etched with a solution of oxalic acid, and the Melt Pool analysis is carried out using an OM on six Single Tracks acquiring each Melt Pool's section with a magnification of 200× to evaluate the variability of the process. The Melt Pool analysis basically consists of the measure of the Melt Pool width and depth that are necessary to calculate the melting regime that governs the Melt Pool formation [42–46]. The reference levels used to evaluate the Melt Pool are those highlighted in [21]. Further indications about the methodology used to perform this analysis are reported in [20].

To assess the effect of the gas flow velocity set point, three values for turbine differential pressure are applied: nominal (relative to the machine adopted in this case study), "low" (−30%), and high (+30%) with respect to the nominal value. The various levels of turbine differential pressure are assessed and investigated in three dedicated jobs.

3. Results and Discussion

3.1. Track Stability Analysis

Figure 3 represents the criteria adopted to evaluate the track stability levels. The stability levels are as follows:

- Not stable.
- Metastable.
- Stable.

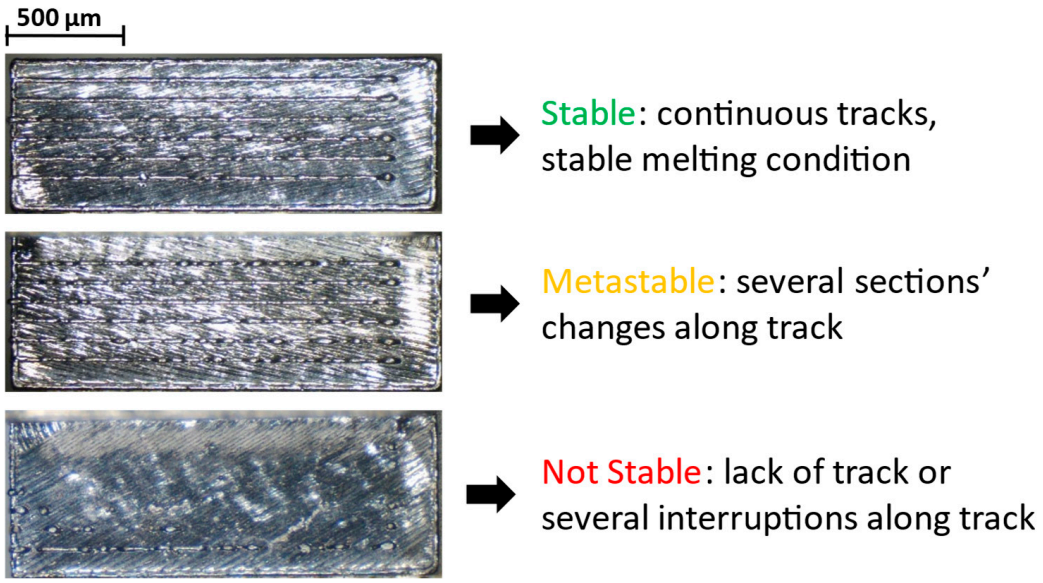

Figure 3. Track stability assessment adopted criteria.

In Table A1, the measured track's stability level for each tested configuration is reported. Figure 4 depicts the scatterplot of the track's stability levels that are measured as a function of the Exposed Area, Position, and Differential Pressure.

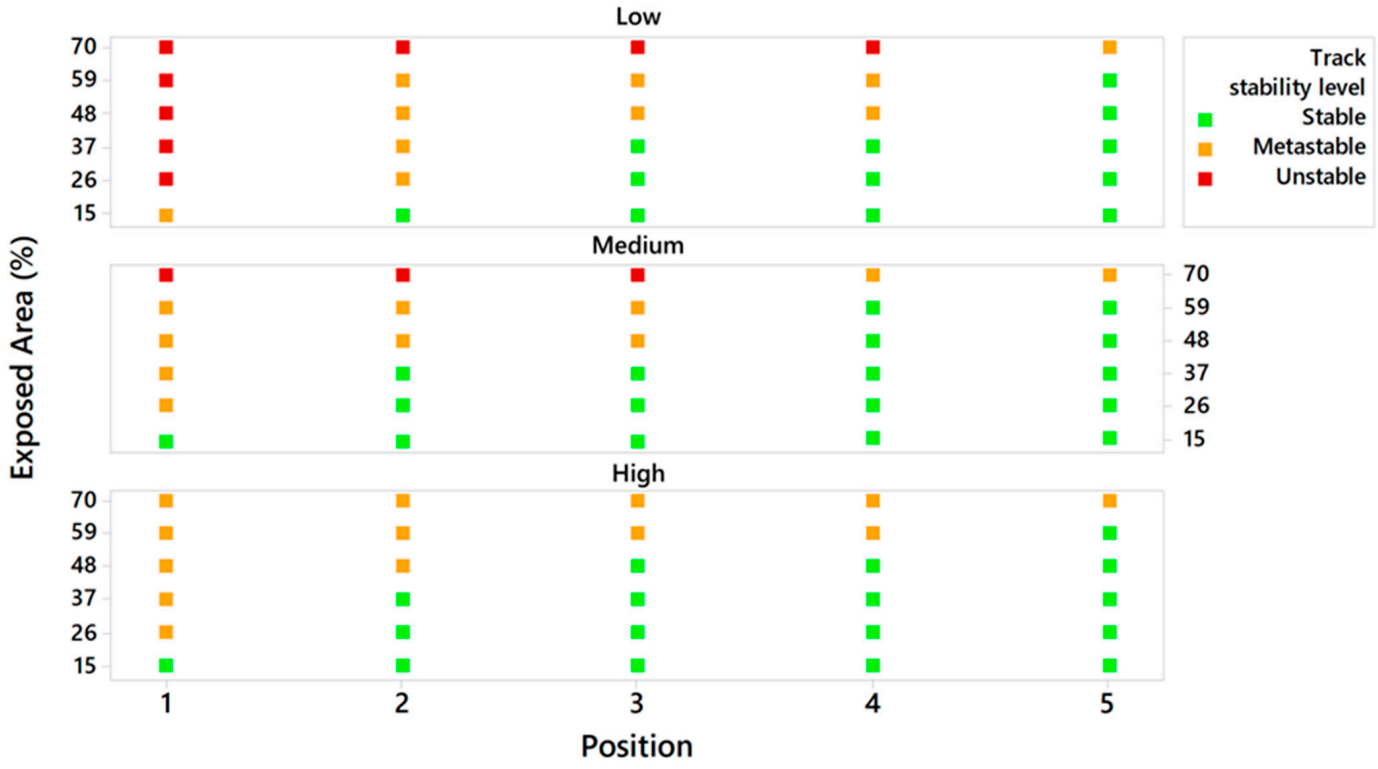

Figure 4. Scatterplot of track's stability level measured as function of Area Exposed (%), Position, and Differential Pressure.

From the scatterplot as shown in Figure 4, it can be observed that the specimens located in position 1 on the building platform are affected by higher process instability with respect to the other positions, resulting in widespread unstable and metastable Single Tracks. It should be noted that the process instability is mitigated by moving to the right side of the building platform, thereby reducing the exposed area, and consequently increasing the

differential pressure, i.e., high gas flow velocity. For instance, considering the scatterplot for a low differential pressure at 37% of the exposed area, it is evident that the Single Track's stability level changes from an unstable condition for position 1 to a stable condition for position 3. Moreover, analyzing the scatterplot for nominal differential pressure and Position 1 condition, it is observed that the Track's stability level changes significantly as a function of the exposed area percentage: moving from an unstable condition for the higher level of exposed area (70%) to a completely stable condition for the lower level (14%). For industrial applications, where maximizing machine productivity requires the utilization of all building platforms, this first result is of remarkable interest.

However, it is clear that the mitigation effect of differential pressure on the Track's stability is appreciable considering Position 2 with an exposed area of 70%, where the Track's stability level changes from an unstable condition to a stable one. It is important to notice that a value of exposed area higher than 50% results in a predominance of unstable or metastable conditions at all the differential pressures investigated.

3.2. Porosity Analysis

Once the Track's stability analysis is completed, the specimens are prepared to perform micrographic analysis. Each specimen is cut, embedded in conductive resin, and polished, using a Strues Secotom-20, Struers CitoPress-30, and Struers Tegramin-30 machines (Struers, Ballerup, Denmark).

Figure 5 shows the box plots of porosity percentage as a function of differential pressure, position and exposed area for the specimens analyzed that are listed in Table A2.

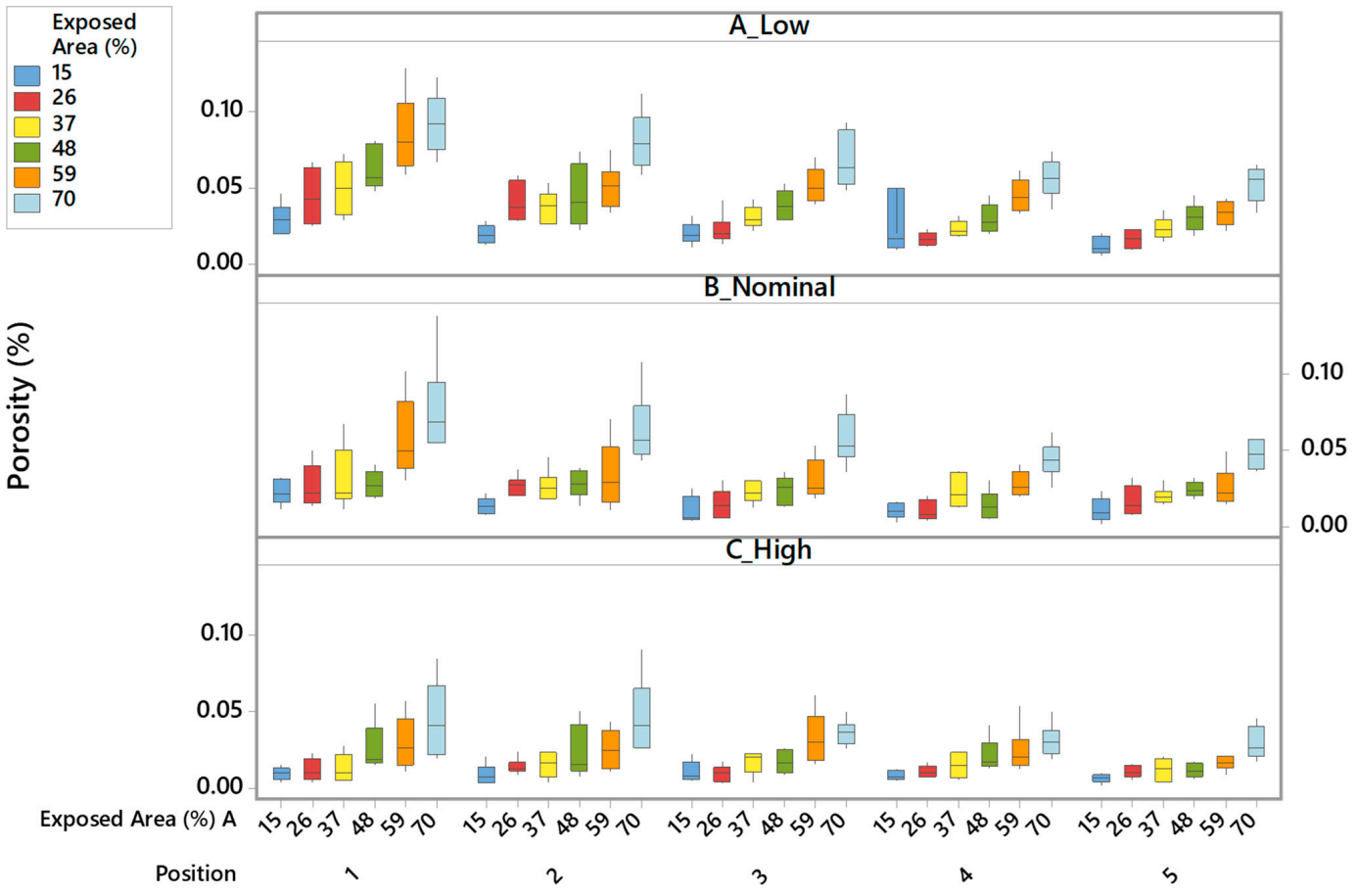

Figure 5. Porosity as a function of exposed area, position, and differential pressure variation.

From Figure 6 it is possible to identify for each tested parameter a distinct and clear main effect by analyzing the percentage of Porosity. As the Differential Pressure is reduced, the material density decreases while moving from the left to the right side of the building platform. On the other hand, reducing the Area Exposed, the material density increases. By evaluating the effect of each parameter individually, it is possible to state that the bottom left region of the building platform in the EOS-M290 machine is a critical zone to print a fully dense material considering Alloy 718. This criticality is primarily caused by the reduction in the laminarity of the shielding gas flow, which in turn leads to turbulent flows. This results in the improper removal of by-products and spatter particles from the powder bed during the melting process. In addition, it is evident that the production of spatter particles is strongly correlated to the size of the Exposed Area on the building platform, meaning that, as the Exposed Area is increased, the higher the formation and concentration of spatter particles on the powder bed become, which hinders the printing of a fully dense material. This is because the spatter particles that are not removed by the recoater and gas flow will accumulate above the powder bed, as shown in Figure 7a, and tend to be melted along with the powder bed in the subsequent layer. Figure 7b shows the SEM image of the powder collected in Zone 2 of Figure 7a. Numerous particles exhibit different morphologies compared to the size distribution of the virgin powder (range between 20 and 63 microns). This morphology can be classified as type 2 sputter particles [52]. The presence of spatter particles may lead to a lack of fusion defects due to a reduced absorption of energy input from the laser source, as indicated in Figure 7c, resulting in an increase in porosity.

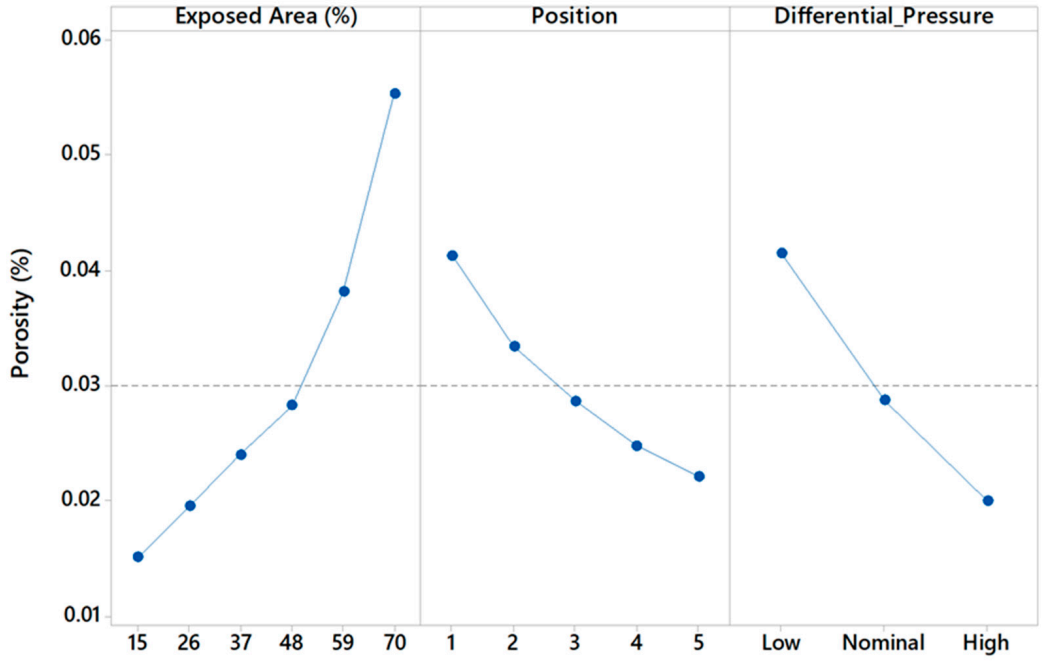

Figure 6. Overview of main effect of each tested parameter on porosity formation.

On the other hand, it is important to highlight by increasing the value of the differential pressure, and consequently the velocity of the gas flow, the removal of spatter particles from the powder bed is enhanced, thus improving the density of the printed material and reducing the presence of defects. Despite all the above-mentioned advantages, care must be taken to avoid any powder denudation effects in other areas of the building platform due to the increased gas flow velocity.

Figure 8 shows the interaction between parameters for porosity formation in the material. From Figure 8, it can be inferred that the interactions between the Exposed Area, Position, and Differential Pressure are either low or zero. No interaction is evident between

the Exposed Area and Differential Pressure. In contrast, a low interaction level is registered between the Position and Exposed Area for some combinations and between the Position and Differential Pressure (i.e., Position 4 and Exposed Area of 14% and 26% and Differential Pressure Nominal and Position 4/5). This result is of utmost interest as it allows each parameter to be optimized separately without influencing the others.

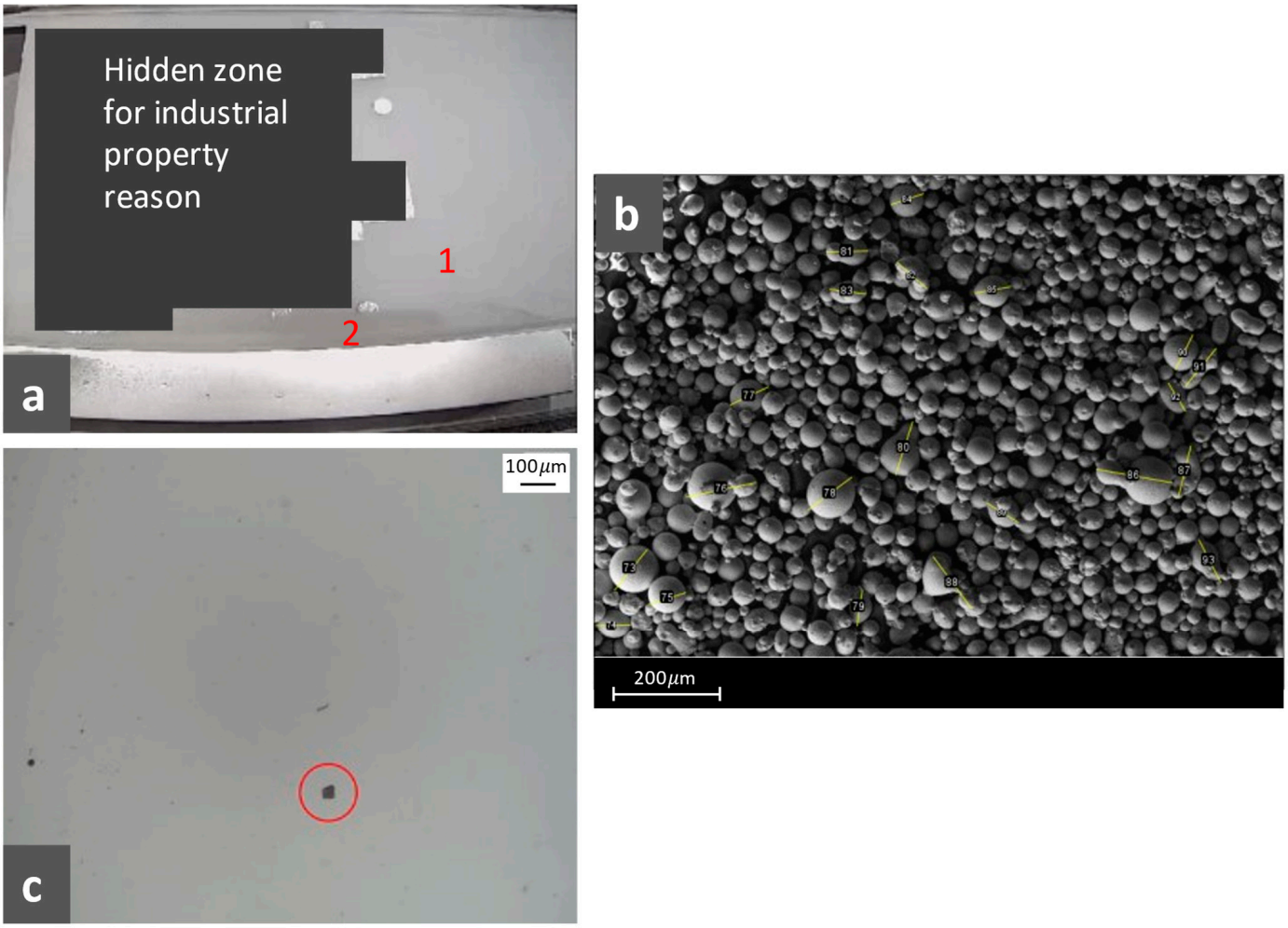

Figure 7. (**a**) Image of the building chamber during the printing process in which the presence of spatter particles above the powder bed is visible as a darker area, zone 2, with respect to the regular powder bed, zone 1; (**b**) SEM image of the powder found in zone 2 with many particles characterized as spatter particles for evidence of larger and/or deformed shape; (**c**) porosity of a zone with Lack of Fusion (LOF) defects probably due to the presence of spatter particles on the powder bed.

Figure 9 illustrates the contour plot to further analyze the effect of Porosity Formation in percentages measured as a function of Exposed Area, Position, and Differential Pressure.

The contour plot shown in Figure 9 demonstrates in terms of area how the high-porosity zone (indicated in dark green) progressively decreases as the differential pressure increases.

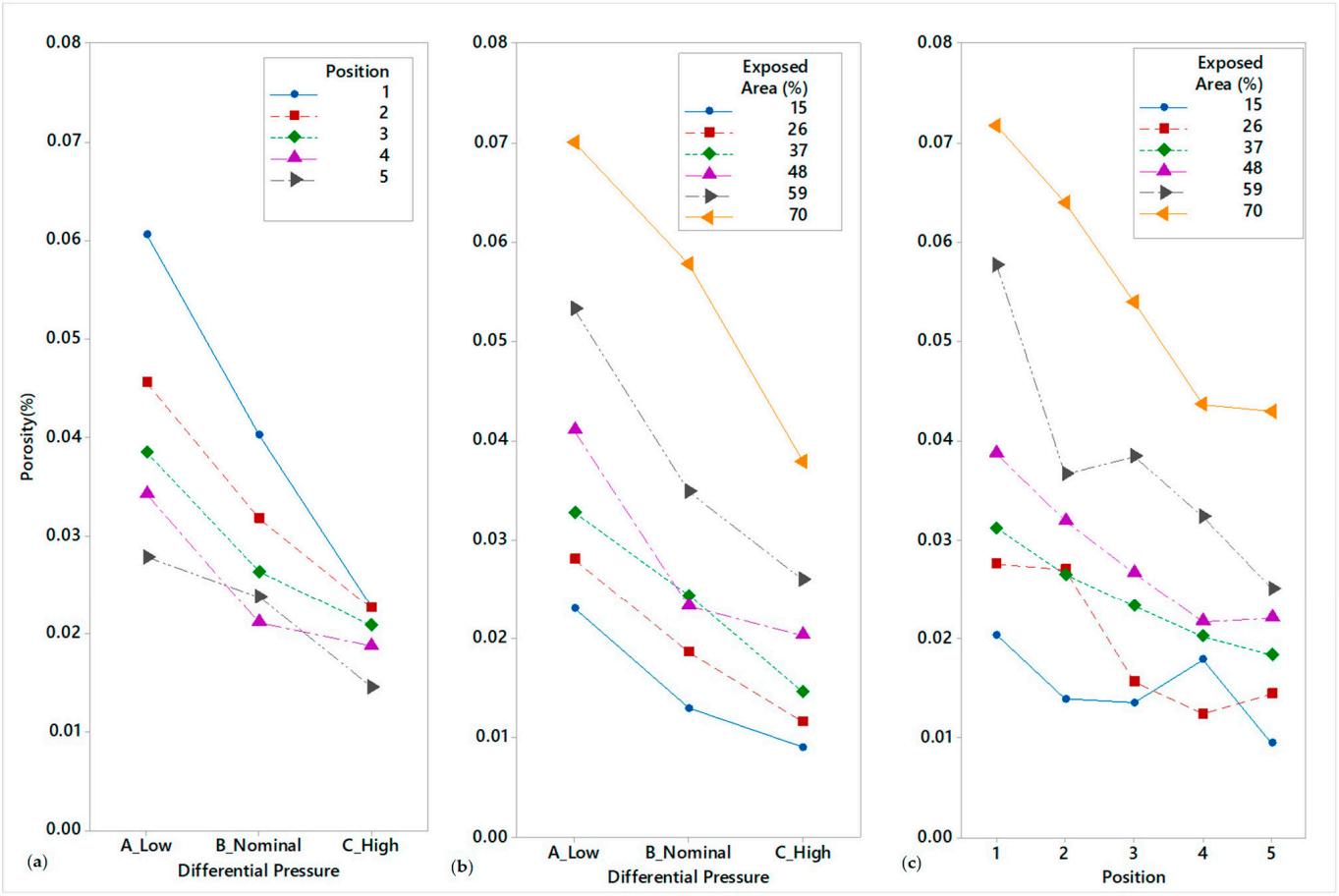

Figure 8. Interaction plots for porosity overview: (**a**) Differential pressure vs. position; (**b**) Differential pressure vs. exposed area; (**c**) Position vs. exposed area.

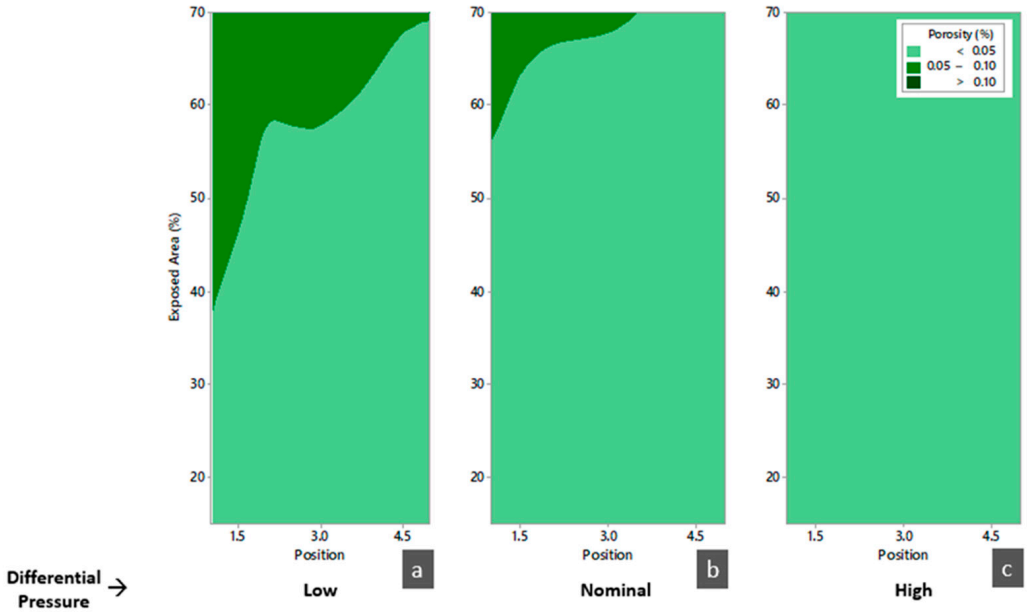

Figure 9. Contour plot of porosity percentage measured as function of exposed area, position and differential pressure: (**a**) Low level; (**b**) Nominal level; (**c**) High level.

3.3. Melt Pool Analysis

Once the porosity analysis is completed, the specimens are etched in the solution of oxalic acid to highlight the Melt Pool boundaries as shown in Figure 10.

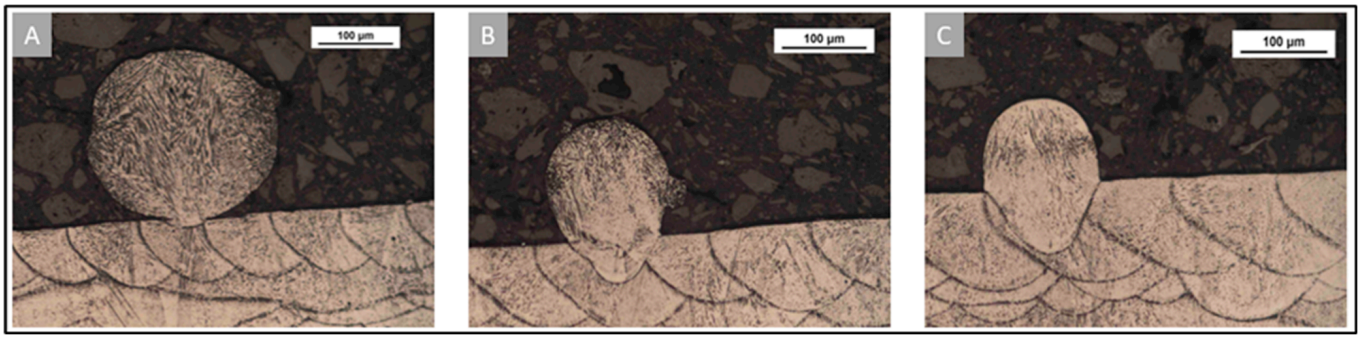

Figure 10. Example of melt pool shape variation as a function of exposed area for position 4 and differential pressure set to nominal value: (**A**) exposed area of 70%; (**B**) exposed area of 59%; (**C**) exposed area of 37%. All images refer to the specimen located at position 1 in Figure 1.

The results of the Melt Pool Depth are shown in Figure 11 (and listed in Table A3) as a function of the tested parameters, and Figure 12 shows the main effect plot to identify the effects of the Exposed Area, Position, and Differential Pressure on the Melt Pool Depth.

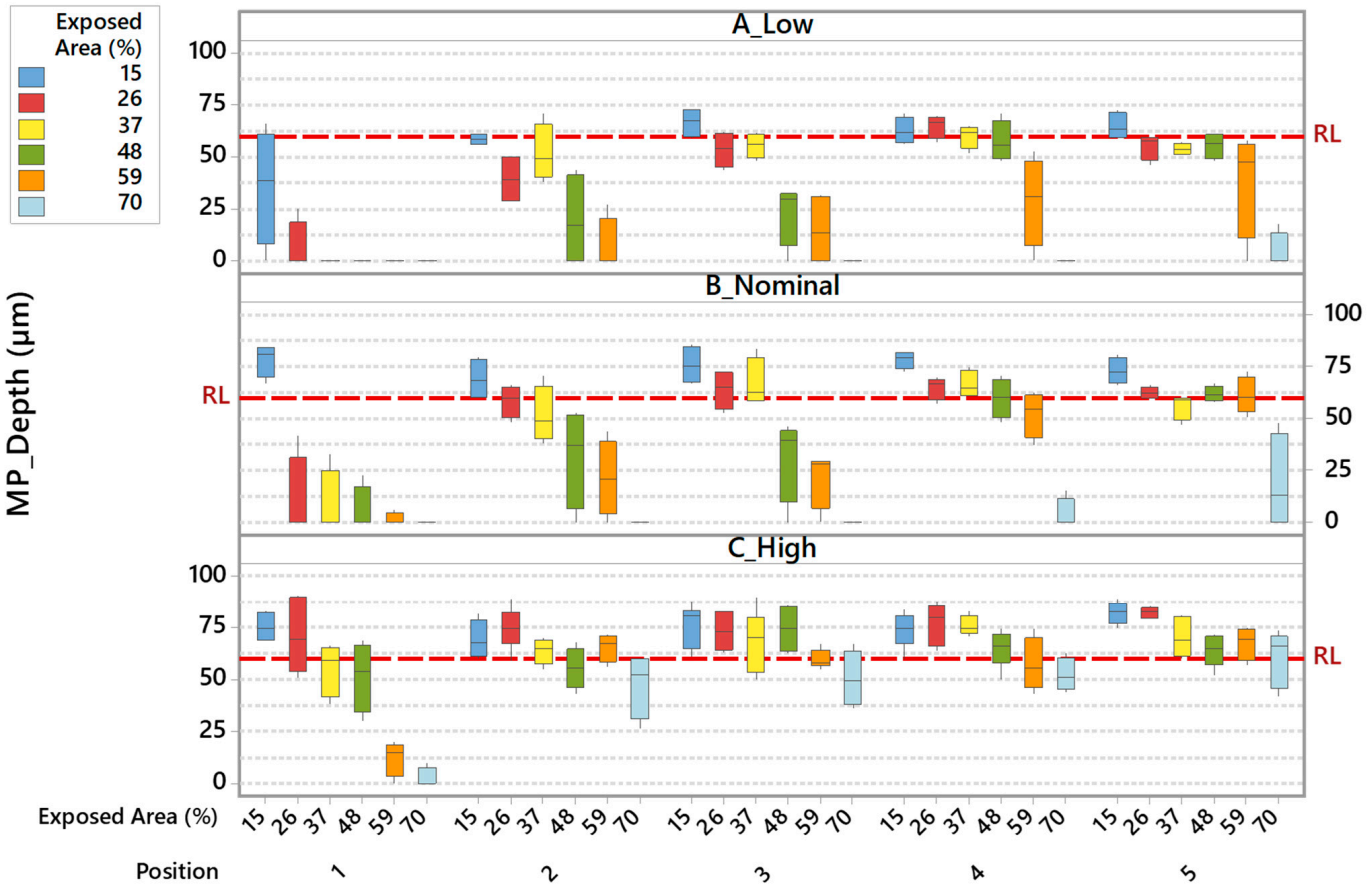

Figure 11. Melt pool depth as a function of exposed area, position and differential pressure variation. The 60 microns reference line (RL) is calculated according to [21].

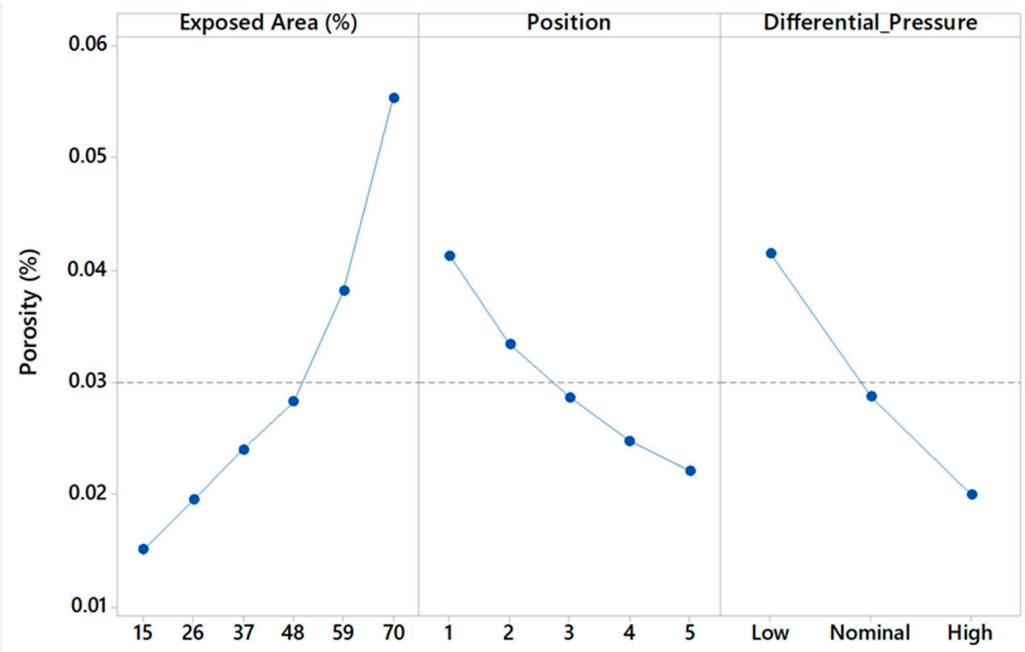

Figure 12. Overview of main effect of exposed area, position and differential pressure on melt pool depth.

Evaluating the main effect plots for the Melt Pool Depth, as shown in Figure 12, for each tested parameter, a distinct and clear main effect is identified. As the Differential Pressure is reduced, the Melt Pool Depth decreases (consequently leading to the remelting of the underlying layer). While on the other hand, moving from the left to the right side of the building platform and reducing the Exposed Area, it should be noted that the Melt Pool Depth increases. These results agree with the Track's stability assessment and Porosity analysis as discussed in the previous section. Furthermore, the considerations that were made for the Porosity analysis are found to be valid also for the Melt Pool Depth analysis. One important aspect that should be noted in this analysis is the way production of spatter particles is increased significantly with the increase in the Exposed Area. On the contrary, lowering the Differential Pressure reduces the laser energy absorptivity of the powder bed that hinders the effective interlayer conductive heat transfer. As a result, a shallow Melt Pool just over 10 microns deep or even absent in some cases leads to a Lack of Fusion melting regime (as shown in Figure 10A,B) during the printing phase.

Figure 13 represents the interaction plot to identify the interactions between Exposed Area, Position, Differential Pressure and Melt Pool Width, respectively. From Figure 13, the results indicate an absent or very low level of interaction between the various parameters on the Melt Pool Width. However, further analysis was performed to verify the main effects on the Melt Pool Width in terms of the same three parameters, taking into account the considerations that were made for the porosity analysis.

The results of the Melt Pool Width are shown in Figure 14 (and listed in Table A3) in terms of Average and Standard deviation.

The main effects plot is shown in Figure 15. The method that was employed to perform the main effects analysis is the same that was employed to evaluate the Melt Pool Depth.

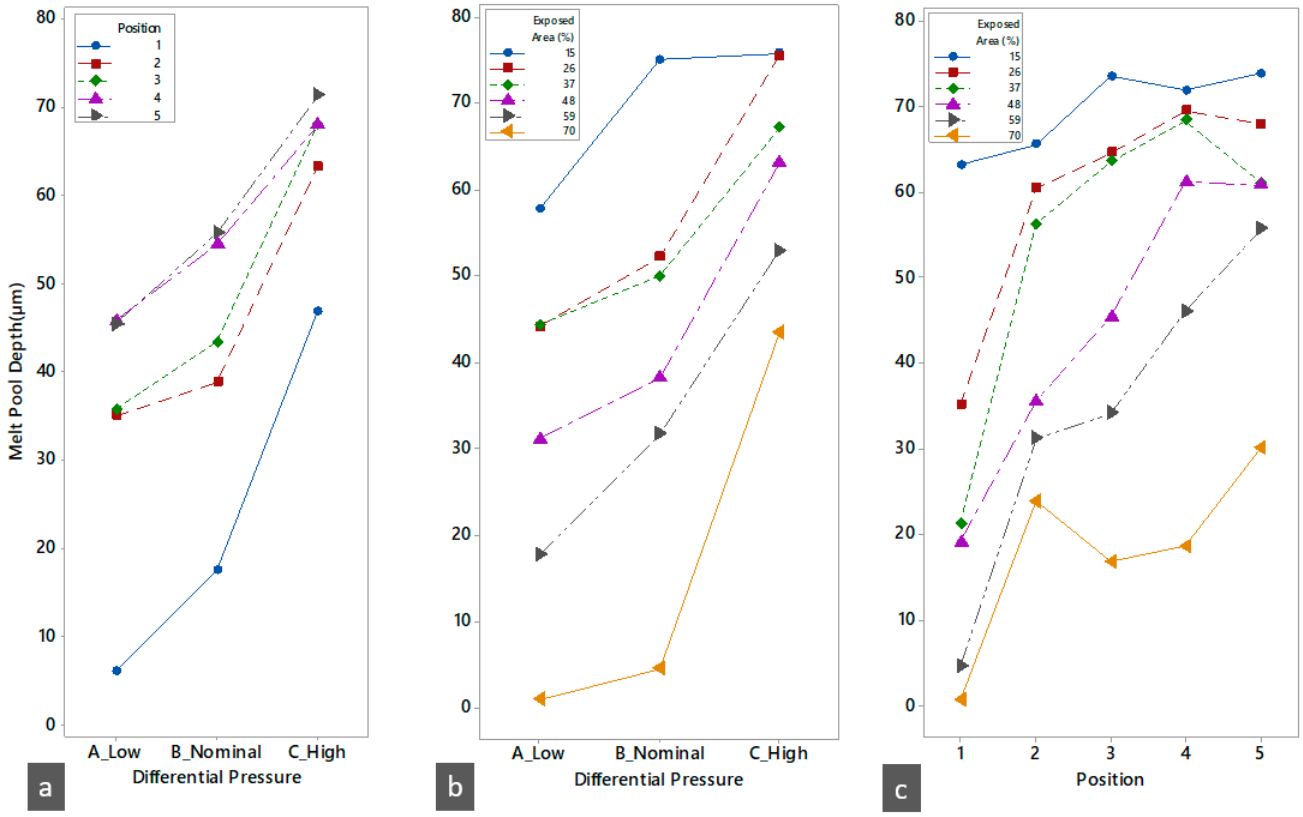

Figure 13. Interaction plots for melt pool depth overview. Interaction plots overview: (**a**) Differential pressure vs. position; (**b**) Differential pressure vs. exposed area; (**c**) Position vs. exposed area.

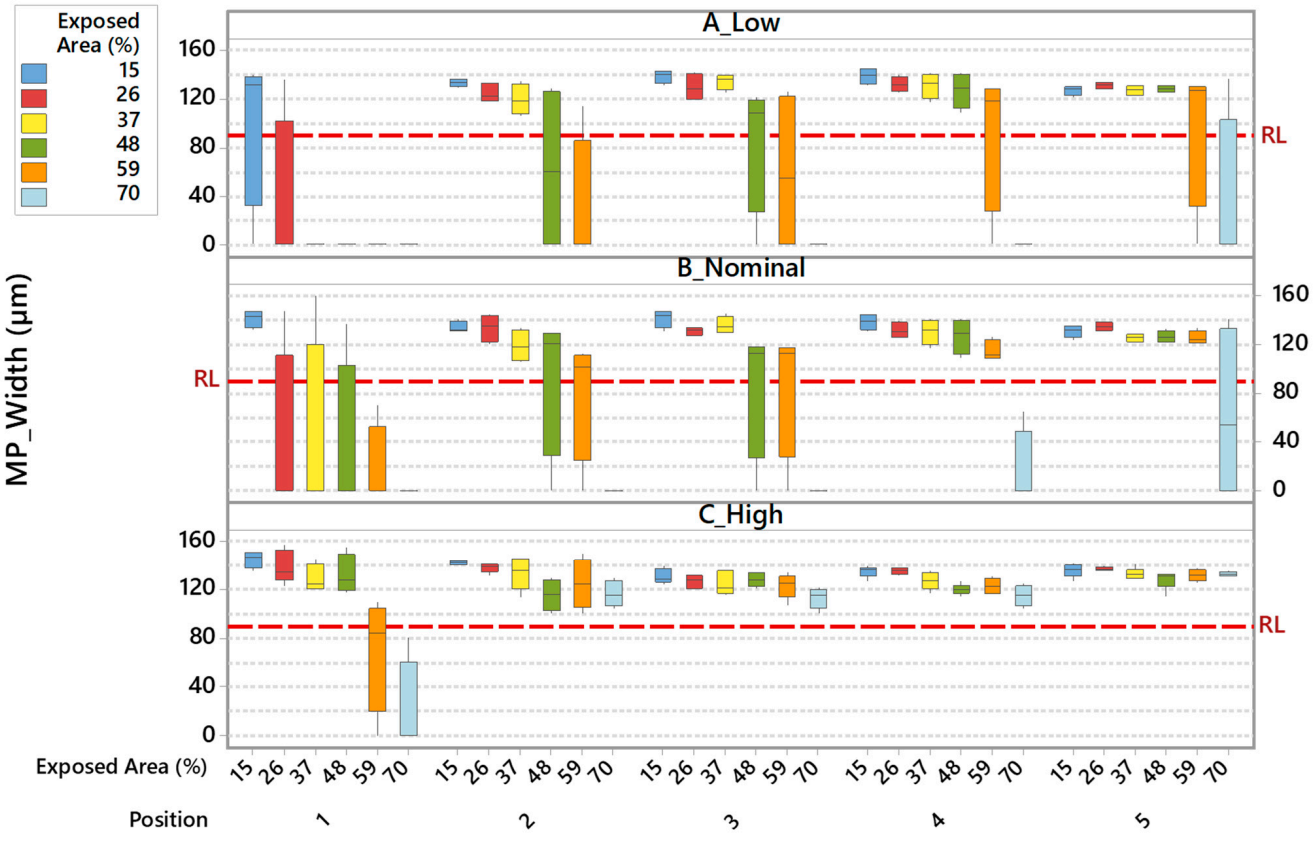

Figure 14. Melt pool width as a function of exposed area, position and differential pressure variation. The 90 microns reference line RL is calculated according to [21].

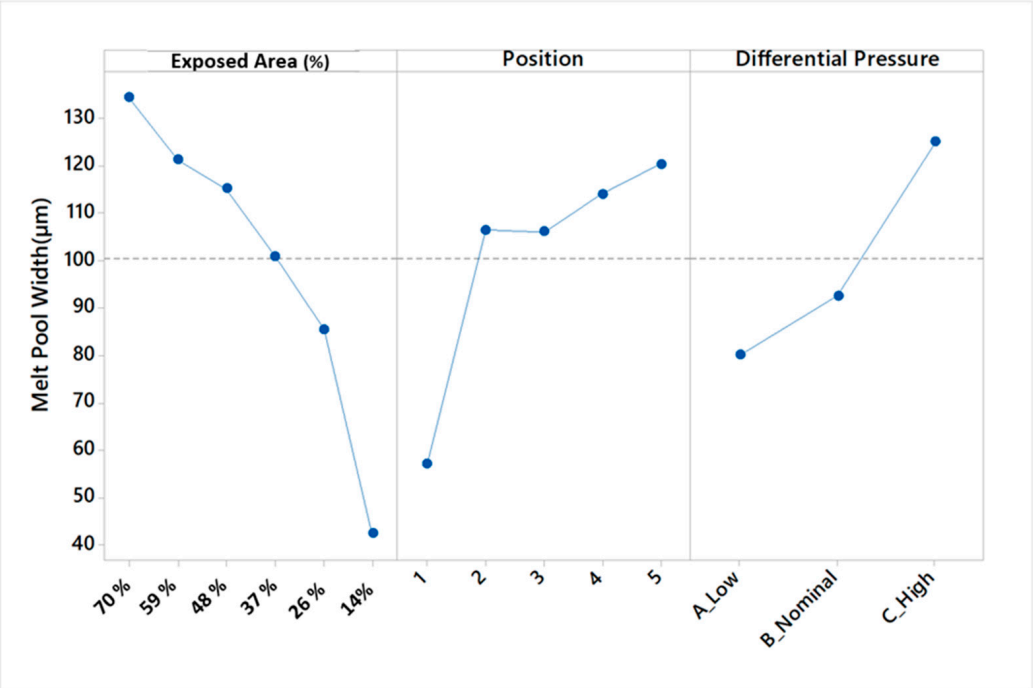

Figure 15. Overview of main effects of exposed area, position and differential pressure on melt pool width.

Evaluating the Main Effect plots for the Melt Pool Width, shown in Figure 15, it is possible to identify for each tested parameter a distinct and clear main effect. As the Differential Pressure is reduced, the Melt Pool Width decreases (consequently resulting in the overlap between adjacent Melt Pools). A similar effect with respect to Melt Pool Depth analysis is observed while moving from the left to the right side of the building platform and reducing the Exposed Area resulting in an increase in the Melt Pool Width. These results agree with those discussed previously about the Track's stability assessment, Porosity analysis, and Melt Pool Depth. Also in this case, the production of spatter particles is increased significantly with the increase in the Exposed Area while lowering the Differential Pressure reduces the laser energy absorptivity of the powder bed that hinders the effective interlayer conductive heat transfer that occurs between adjacent Melt Pools. Due to these boundary conditions, either a shallow Melt Pool or even the absence of one in some cases (as shown in Figure 10A,B) can be observed during the printing phase.

Figure 16 shows the Interaction plot between the Exposed Area, Position, and Differential Plot for the Melt Pool Width. From the analysis, it is evident the interactions within the different parameters are low and there is a zero level of interaction in some cases. As discussed in the Melt Pool Depth analysis, no interaction is observed between the Exposed Area and Differential Pressure, and between the Position and Differential Pressure. However, a low interaction level is observed between the Position and Exposed Area for certain combinations (i.e., Position 3 and 5 and Exposed Area of 14%, 26%, and 37%).

In Figures 17 and 18, the contour plot for the Melt Pool Depth and Width as a function of the Exposed Area, Position, and Differential Pressure, respectively, is illustrated.

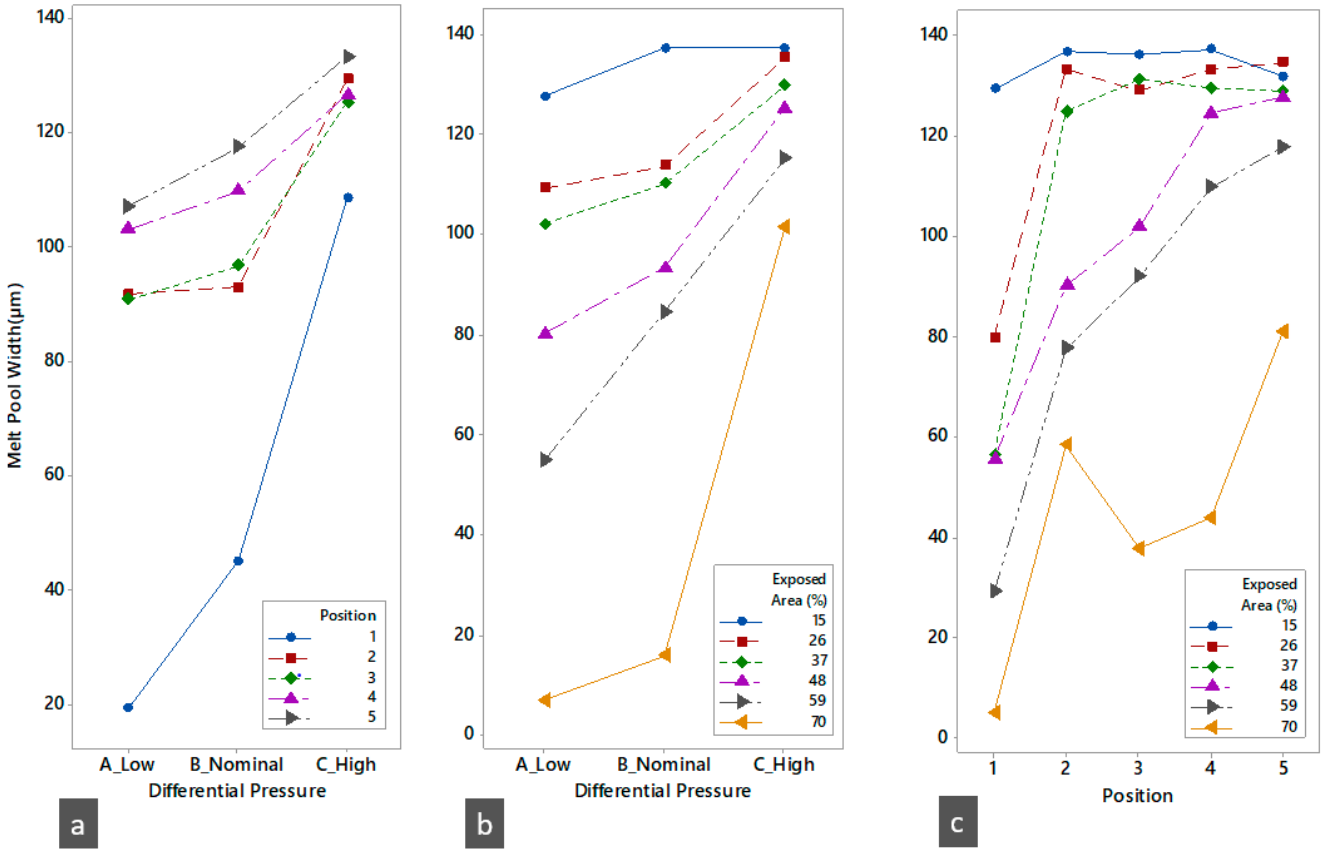

Figure 16. Interaction plots for melt pool width overview. Interaction plots overview: (**a**) Differential pressure vs. position; (**b**) Differential pressure vs. exposed area; (**c**) Position vs. exposed area.

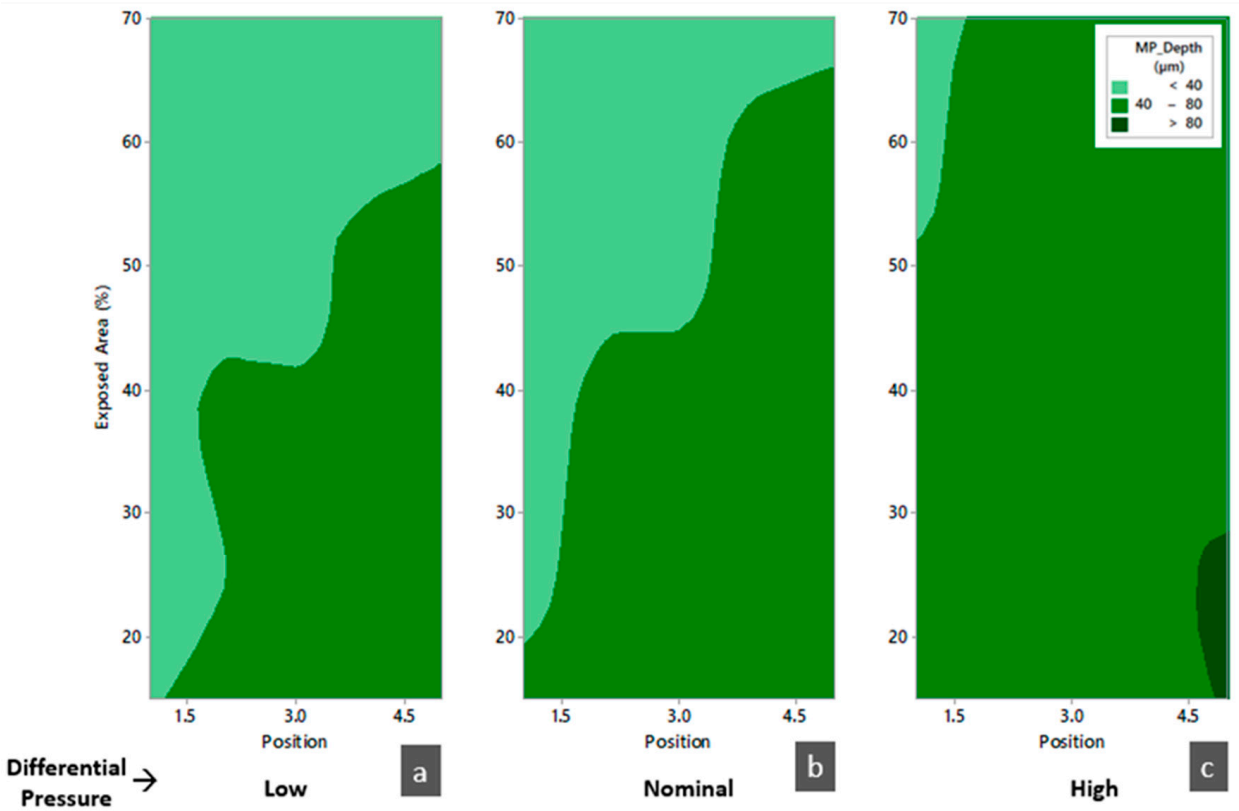

Figure 17. Contour plot of melt pool depth as function of exposed area, position and differential pressure: (**a**) Low level; (**b**) Nominal level; (**c**) High level.

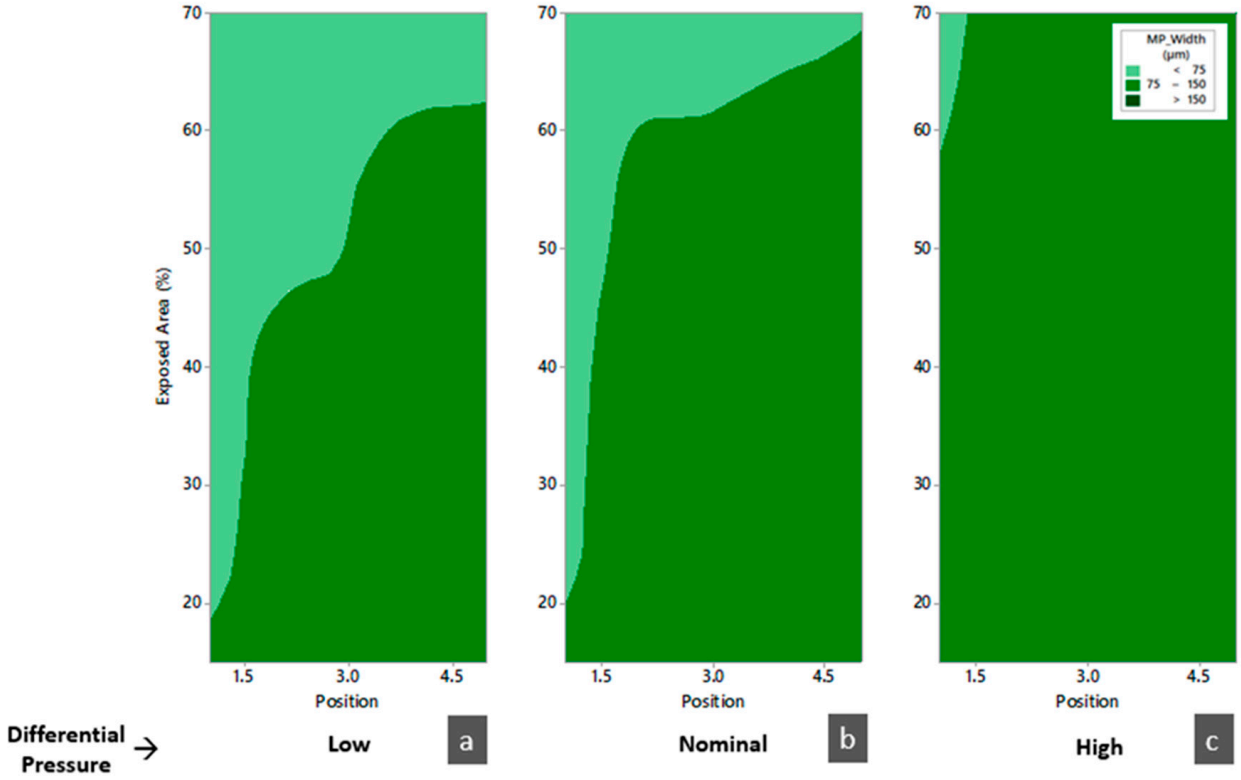

Figure 18. Contour plot of melt pool width as a function of exposed area, position and differential pressure: (**a**) Low level; (**b**) Nominal level; (**c**) High level.

From Figure 17, the Melt Pool Depth is shown in a progressive manner. The light green zones indicate a shallow Melt Pool while the dark green areas indicate the contrary. It should be that the area of the shallow Melt Pool progressively decreases as the Differential Pressure increases. These studies confirm the validity of the previous analyses performed with respect to Track Stability and Porosity Analysis.

Figure 18 represents the contour plot of the Melt Pool width as a function of the Exposed Area, Position, and Differential Pressure. The light green zones indicate a narrow Melt Pool while the dark green areas indicate the contrary. The same trend observed for the Melt Pool Depth is observed also for the Melt Pool Width in terms of increasing the Differential Pressure, i.e., the area of the narrow Melt Pool progressively decreases as the Differential Pressure increases.

4. Conclusions

This work elucidates and quantifies the entity of the building platform inhomogeneities in the PBF-LB/M process through the evaluation of the Track's stability level and Melt Pool of several Single Tracks. Moreover, the density and defect distribution inside the material have also been measured.

It is possible to highlight how each process parameter that was evaluated, i.e., Exposed Area (%), Position on building platform, and Differential Pressure, has a main effect on the building platform inhomogeneities. In particular:

- The Exposed Area increase promotes Single Track instability, loss of conductive regime and defect formation;
- Criticality for printability of Alloy 718 in the EOS M290 machine at the position closed to the outlet nozzle and in general when the Exposed Area is more than about 50% of the build platform has been detected;

- A mitigation is possible increasing the value of the Differential Pressure and thus shielding the gas flow velocity, facilitating the removal of the melting's subproducts, such as spatter particles;
- The interaction between the parameters is quite low or null, allowing us to optimize each one without having any effect on the other.

In conclusion, this investigation remarks on some criticality for the printability of Allot 718 in the EOS M290 machine; the mitigation suggested by experimental results can improve the Track's and the Melt Pool's stability, allowing the manufacture of a defect-free and fully dense material. The results shown allow for suggestions on how to use the printing platform during job definitions when there is a need to maximize its use.

A critical aspect to be considered, as a result of the increased gas flow velocity, could be a partial denudation of the powder in the building platform area near to the gas flow nozzle inlet. In future work, this critical aspect will be investigated in order to evaluate the robustness of the proposed mitigation solution on printability inhomogeneities on the PBF-LB/M process.

Author Contributions: Conceptualization, N.B., L.C., M.P., A.G. and P.C.; methodology, L.C., M.M., A.G. and M.P.; software, N.B., L.C. and M.M.; validation, M.M. and M.P.; formal analysis, N.B., L.C., and A.G.; investigation, N.B., L.C. and A.G.; resources, M.P.; data curation, N.B., M.M. and A.G.; writing—original draft preparation, N.B., L.C. and A.G.; writing—review and editing, N.B., L.C., M.M., A.G., G.A. and P.C.; visualization, N.B., L.C. and A.G.; supervision, M.P., A.G. and P.C.; project administration, M.P.; funding acquisition, M.P. All authors have read and agreed to the published version of the manuscript.

Funding: This research received no external funding.

Institutional Review Board Statement: Not applicable.

Informed Consent Statement: Not applicable.

Data Availability Statement: Summarized data are contained within the article. The raw data are available on request from the corresponding author after obtaining the permission of Baker Hughes, Nuovo Pignone.

Conflicts of Interest: Authors Niccolo Baldi, Lokesh Chandrabalan, Marco Manetti, and Marco Palladino were employed by the company Baker Hughes, Nuovo Pignone. The remaining authors declare that the research was conducted in the absence of any commercial or financial relationships that could be construed as a potential conflict of interest.

Appendix A

The appendix shows the data used for the paper; in particular, in Table A1 the data obtained as regards the track stability level as a function of Differential Pressure, Position and Exposed Area are reported; in Table A2, the data of Porosity and in Table A3 the analysis of the Melt Pool Depth and Width are given.

Table A1. Track stability level tracking table.

Differential Pressure	Position	Exposed Area (%)	Track Stability Level
Low	1	70	Unstable
Low	1	59	Unstable
Low	1	48	Unstable
Low	1	37	Unstable
Low	1	26	Unstable
Low	1	14	Metastable
Low	2	70	Unstable

Table A1. *Cont.*

Differential Pressure	Position	Exposed Area (%)	Track Stability Level
Low	2	59	Metastable
Low	2	48	Metastable
Low	2	37	Metastable
Low	2	26	Metastable
Low	2	14	Stable
Low	3	70	Not stable
Low	3	59	Metastable
Low	3	48	Metastable
Low	3	37	Stable
Low	3	26	Stable
Low	3	14	Stable
Low	4	70	Unstable
Low	4	59	Metastable
Low	4	48	Metastable
Low	4	37	Stable
Low	4	26	Stable
Low	4	14	Stable
Low	5	70	Metastable
Low	5	59	Stable
Low	5	48	Stable
Low	5	37	Stable
Low	5	26	Stable
Low	5	14	Stable
Nominal	1	70	Unstable
Nominal	1	59	Metastable
Nominal	1	48	Metastable
Nominal	1	37	Metastable
Nominal	1	26	Metastable
Nominal	1	14	Stable
Nominal	2	70	Unstable
Nominal	2	59	Metastable
Nominal	2	48	Metastable
Nominal	2	37	Stable
Nominal	2	26	Stable
Nominal	2	14	Stable
Nominal	3	70	Unstable
Nominal	3	59	Metastable
Nominal	3	48	Metastable
Nominal	3	37	Stable
Nominal	3	26	Stable
Nominal	3	14	Stable
Nominal	4	70	Metastable
Nominal	4	59	Stable
Nominal	4	48	Stable
Nominal	4	37	Stable
Nominal	4	26	Stable
Nominal	4	14	Stable
Nominal	5	70	Metastable
Nominal	5	59	Stable
Nominal	5	48	Stable
Nominal	5	37	Stable
Nominal	5	26	Stable
Nominal	5	14	Stable
High	1	70	Metastable
High	1	59	Metastable

Table A1. *Cont.*

Differential Pressure	Position	Exposed Area (%)	Track Stability Level
High	1	48	Metastable
High	1	37	Metastable
High	1	26	Metastable
High	1	14	Stable
High	2	70	Metastable
High	2	59	Metastable
High	2	48	Metastable
High	2	37	Stable
High	2	26	Stable
High	2	14	Stable
High	3	70	Metastable
High	3	59	Metastable
High	3	48	Stable
High	3	37	Stable
High	3	26	Stable
High	3	14	Stable
High	4	70	Metastable
High	4	59	Metastable
High	4	48	Stable
High	4	37	Stable
High	4	26	Stable
High	4	14	Stable
High	5	70	Metastable
High	5	59	Stable
High	5	48	Stable
High	5	37	Stable
High	5	26	Stable
High	5	14	Stable

Table A2. Porosity analysis tracking table.

Differential Pressure	Position	Exposed Area (%)	Porosity (%)	
			Avg.	SD
Low	1	70	0.093	0.020
Low	1	59	0.086	0.023
Low	1	48	0.062	0.014
Low	1	37	0.051	0.018
Low	1	26	0.045	0.018
Low	1	14	0.029	0.010
Low	2	70	0.082	0.020
Low	2	59	0.051	0.015
Low	2	48	0.045	0.020
Low	2	37	0.038	0.011
Low	2	26	0.041	0.013
Low	2	14	0.019	0.006
Low	3	70	0.068	0.018
Low	3	59	0.052	0.012
Low	3	48	0.039	0.009
Low	3	37	0.031	0.007
Low	3	26	0.023	0.010
Low	3	14	0.019	0.007
Low	4	70	0.056	0.013
Low	4	59	0.045	0.011

Table A2. *Cont.*

Differential Pressure	Position	Exposed Area (%)	Porosity (%)	
			Avg.	SD
Low	4	48	0.029	0.010
Low	4	37	0.023	0.005
Low	4	26	0.016	0.004
Low	4	14	0.015	0.005
Low	5	70	0.052	0.012
Low	5	59	0.033	0.008
Low	5	48	0.031	0.009
Low	5	37	0.023	0.007
Low	5	26	0.016	0.006
Low	5	14	0.011	0.006
Nominal	1	70	0.077	0.031
Nominal	1	59	0.057	0.027
Nominal	1	48	0.027	0.014
Nominal	1	37	0.031	0.022
Nominal	1	26	0.026	0.014
Nominal	1	14	0.022	0.008
Nominal	2	70	0.064	0.024
Nominal	2	59	0.033	0.022
Nominal	2	48	0.027	0.009
Nominal	2	37	0.026	0.010
Nominal	2	26	0.026	0.006
Nominal	2	14	0.016	0.006
Nominal	3	70	0.057	0.018
Nominal	3	59	0.031	0.013
Nominal	3	48	0.024	0.009
Nominal	3	37	0.022	0.007
Nominal	3	26	0.014	0.009
Nominal	3	14	0.010	0.009
Nominal	4	70	0.043	0.013
Nominal	4	59	0.027	0.010
Nominal	4	48	0.014	0.009
Nominal	4	37	0.023	0.011
Nominal	4	26	0.010	0.005
Nominal	4	14	0.009	0.007
Nominal	5	70	0.047	0.010
Nominal	5	59	0.025	0.013
Nominal	5	48	0.024	0.006
Nominal	5	37	0.020	0.006
Nominal	5	26	0.016	0.010
Nominal	5	14	0.009	0.008
High	1	70	0.045	0.025
High	1	59	0.031	0.017
High	1	48	0.025	0.016
High	1	37	0.014	0.009
High	1	26	0.012	0.008
High	1	14	0.009	0.004
High	2	70	0.047	0.024
High	2	59	0.026	0.013
High	2	48	0.024	0.017
High	2	37	0.016	0.008
High	2	26	0.015	0.005
High	2	14	0.011	0.006
High	3	70	0.039	0.014
High	3	59	0.033	0.017

Table A2. *Cont.*

Differential Pressure	Position	Exposed Area (%)	Porosity (%)	
			Avg.	SD
High	3	48	0.019	0.007
High	3	37	0.017	0.007
High	3	26	0.010	0.005
High	3	14	0.009	0.006
High	4	70	0.031	0.011
High	4	59	0.025	0.014
High	4	48	0.022	0.011
High	4	37	0.015	0.008
High	4	26	0.011	0.004
High	4	14	0.009	0.003
High	5	70	0.029	0.011
High	5	59	0.016	0.005
High	5	48	0.012	0.005
High	5	37	0.011	0.007
High	5	26	0.010	0.004
High	5	14	0.007	0.003

Table A3. Melt pool analysis tracking table.

Differential Pressure (mbar)	Position	Exposed Area (%)	Depth (μm)		Width (μm)	
			Avg.	SD	Avg.	SD
Low	1	70	0.0	0.0	0.0	0.0
Low	1	59	0.0	0.0	0.0	0.0
Low	1	48	0.0	0.0	0.0	0.0
Low	1	37	0.0	0.0	0.0	0.0
Low	1	26	6.25	12.5	34.0	68
Low	1	14	35.8	27.6	100.7	67.3
Low	2	70	0.0	0.0	0.0	0.0
Low	2	59	19.5	22.9	61.7	71.4
Low	2	48	51.7	13.9	119.0	13.2
Low	2	37	29.5	21.5	93.2	7.8
Low	2	26	58.5	2.4	133.2	3.3
Low	3	14	0.0	0.0	0.0	0.0
Low	3	70	14.8	17.1	58.7	68.2
Low	3	59	23.0	15.4	84.2	56.6
Low	3	48	55.5	5.8	134.1	6.5
Low	3	37	53.8	8.6	129.5	10.8
Low	3	26	66.8	6.8	138.5	5.3
Low	4	14	0.0	0.0	0.0	0.0
Low	4	70	28.8	21.8	91.2	61.4
Low	4	59	57.5	9.9	127	14.8
Low	4	48	60.2	5.7	130.7	10.4
Low	4	37	65.0	5.6	131.7	6.4
Low	4	26	62.8	6.3	138.2	6.2
Low	5	14	4.5	9.1	34.1	68.5
Low	5	70	38.2	26.1	95.7	63.9
Low	5	59	55.4	6.1	128.0	3.2
Low	5	48	54.0	2.6	126.7	4.1
Low	5	37	55.2	6.4	131	2.9
Low	5	26	64.8	6.2	127	4.1
Nominal	1	14	0.0	0.0	0.0	0.0
Nominal	1	70	1.5	3.0	17.5	35

Table A3. *Cont.*

Differential Pressure (mbar)	Position	Exposed Area (%)	Depth (μm)		Width (μm)	
			Avg.	SD	Avg.	SD
Nominal	1	59	5.8	11.5	34.25	68.5
Nominal	1	48	8.2	16.5	40.0	80.0
Nominal	1	37	42.0	21.0	37.0	74.0
Nominal	1	26	78.5	7.9	141.2	6.9
Nominal	2	14	0.0	0.0	0.0	0.0
Nominal	2	70	21.5	18.3	79.0	53.1
Nominal	2	59	31.8	24.2	92.7	62.1
Nominal	2	48	51.7	13.9	119.1	13.2
Nominal	2	37	58.5	7.9	133.7	11.1
Nominal	2	26	69.25	9.8	134.2	4.6
Nominal	3	14	0.0	0.0	0.0	0.0
Nominal	3	70	21.5	14.4	86.0	57.4
Nominal	3	59	31.3	21.1	86.0	57.4
Nominal	3	48	67.0	11.8	135.7	7.3
Nominal	3	37	64.2	9.1	131.2	3.4
Nominal	3	26	76.1	9.0	141.5	7.2
Nominal	4	14	3.8	7.5	16.2	32.5
Nominal	4	70	52.5	11.1	114.7	8.3
Nominal	4	59	60.0	9.6	127.0	14.8
Nominal	4	48	66.5	6.8	130.7	10.4
Nominal	4	37	65.2	5.6	131.7	6.4
Nominal	4	26	78.5	4.1	138.5	6.2
Nominal	5	14	18.7	23.2	62.5	73.3
Nominal	5	70	61.2	9.1	125.5	5.9
Nominal	5	59	62.0	3.7	126.5	5.1
Nominal	5	48	59.5	6.2	125.2	3.4
Nominal	5	37	62.8	2.7	134.7	3.9
Nominal	5	26	73.1	6.5	131.2	5.1
High	1	14	2.5	5.0	20.2	40.5
High	1	70	12.2	8.6	70.0	48.3
High	1	59	51.8	16.9	132.5	16.5
High	1	48	55.5	12.8	129.2	11.6
High	1	37	71.1	16.8	138.8	13.4
High	1	26	75.5	7.04	145.7	7.1
High	2	14	47.8	16.1	116.7	10.4
High	2	70	65.1	8.2	125.2	21.1
High	2	59	58.2	10.2	116.1	13.0
High	2	48	63.6	6.1	134	13.5
High	2	37	74.8	10.6	138.4	3.8
High	2	26	67.6	8.8	139.6	7.3
High	3	14	50.5	13.2	113.5	8.9
High	3	70	60.1	4.6	123.4	10.3
High	3	59	74.8	10.8	128.6	5.9
High	3	48	67.4	15.3	125.4	9.5
High	3	37	73.6	9.3	126.8	5.6
High	3	26	79.6	8.2	131.8	6.6
High	4	14	52.2	8.1	115.5	8.3
High	4	70	57.2	13.2	123.5	6.5
High	4	59	65.2	9.3	120.4	4.3
High	4	48	76.4	4.7	127.4	7.2
High	4	37	76.9	10.4	135.6	2.7
High	4	26	74.2	8.8	135.2	4.9
High	5	14	59.8	13.6	133.2	1.9
High	5	70	67.8	8.1	132.1	5.2

Table A3. *Cont.*

Differential Pressure (mbar)	Position	Exposed Area (%)	Depth (µm)		Width (µm)	
			Avg.	SD	Avg.	SD
High	5	59	64.2	7.9	128.4	7.6
High	5	48	70.6	9.6	133.4	4.6
High	5	37	82.4	2.9	137.2	1.9
High	5	26	82.0	5.3	136.0	5.7

References

1. Blakey-Milner, B.; Gradl, P.; Snedden, G.; Brooks, M.; Pitot, J.; Lopez, E.; Leary, M.; Berto, F.; Du Plessis, A. Metal Additive Manufacturing in Aerospace: A Review. *Mater. Des.* **2021**, *209*, 110008. [CrossRef]
2. Amano, H.; Ishimoto, T.; Hagihara, K.; Suganuma, R.; Aiba, K.; Sun, S.-H.; Wang, P.; Nakano, T. Impact of Gas Flow Direction on the Crystallographic Texture Evolution in Laser Beam Powder Bed Fusion. *Virtual Phys. Prototyp.* **2023**, *18*, e2169172. [CrossRef]
3. Wang, Z.; Guan, K.; Gao, M.; Li, X.; Chen, X.; Zeng, X. The Microstructure and Mechanical Properties of Deposited-IN718 by Selective Laser Melting. *J. Alloys Compd.* **2011**, *513*, 518–523. [CrossRef]
4. Osakada, K.; Shiomi, M. Flexible Manufacturing of Metallic Products by Selective Laser Melting of Powder. *Int. J. Mach. Tools Manuf.* **2006**, *46*, 1188–1193. [CrossRef]
5. Kruth, J.; Mercelis, P.; Van Vaerenbergh, J.; Froyen, L.; Rombouts, M. Binding Mechanisms in Selective Laser Sintering and Selective Laser Melting. *Rapid Prototyp. J.* **2005**, *11*, 26–36. [CrossRef]
6. Yadroitsev, I.; Gusarov, A.; Yadroitsava, I.; Smurov, I. Single Track Formation in Selective Laser Melting of Metal Powders. *J. Mater. Process. Technol.* **2010**, *210*, 1624–1631. [CrossRef]
7. Hagedorn, Y. *Laser Additive Manufacturing of Ceramic Components*; Elsevier: Amsterdam, The Netherlands, 2016; pp. 163–180.
8. Smith, J.; Xiong, W.; Yan, W.; Lin, S.; Cheng, P.; Kafka, O.L.; Wagner, G.J.; Cao, J.; Liu, W.K. Linking Process, Structure, Property, and Performance for Metal-Based Additive Manufacturing: Computational Approaches with Experimental Support. *Comput. Mech.* **2016**, *57*, 583–610. [CrossRef]
9. Jo, A.R.; An, J.S.; Kim, S.H.; Park, D.Y.; Moon, Y.H.; Hwang, S.K. Optimal Process Conditions for Powder Bed Fusion and Analysis of Properties of Maraging Steel. *Met. Mater. Int.* **2023**, *29*, 2865–2877. [CrossRef]
10. Metelkova, J.; Kinds, Y.; Kempen, K.; De Formanoir, C.; Witvrouw, A.; Van Hooreweder, B. On the Influence of Laser Defocusing in Selective Laser Melting of 316L. *Addit. Manuf.* **2018**, *23*, 161–169. [CrossRef]
11. Gokcekaya, O.; Ishimoto, T.; Nishikawa, Y.; Kim, Y.S.; Matsugaki, A.; Ozasa, R.; Weinmann, M.; Schnitter, C.; Stenzel, M.; Kim, H.S.; et al. Novel Single Crystalline-like Non-Equiatomic TiZrHfNbTaMo Bio-High Entropy Alloy (BioHEA) Developed by Laser Powder Bed Fusion. *Mater. Res. Lett.* **2022**, *11*, 274–280. [CrossRef]
12. Liu, S.Y.; Li, H.Q.; Qin, C.X.; Zong, R.; Fang, X.Y. The Effect of Energy Density on Texture and Mechanical Anisotropy in Selective Laser Melted Inconel 718. *Mater. Des.* **2020**, *191*, 108642. [CrossRef]
13. Ekubaru, Y.; Gokcekaya, O.; Ishimoto, T.; Sato, K.; Manabe, K.; Wang, P.; Nakano, T. Excellent Strength–Ductility Balance of Sc-Zr-Modified Al–Mg Alloy by Tuning Bimodal Microstructure via Hatch Spacing in Laser Powder Bed Fusion. *Mater. Des.* **2022**, *221*, 110976. [CrossRef]
14. Ishimoto, T.; Hagihara, K.; Hisamoto, K.; Sun, S.-H.; Nakano, T. Crystallographic Texture Control of Beta-Type Ti–15Mo–5Zr–3Al Alloy by Selective Laser Melting for the Development of Novel Implants with a Biocompatible Low Young's Modulus. *Scr. Mater.* **2017**, *132*, 34–38. [CrossRef]
15. Ren, Y.; Liang, L.; Shan, Q.; Cai, A.; Du, J.; Huang, Q.; Liu, S.; Yang, X.; Tian, Y.; Wu, H. Effect of Volumetric Energy Density on Microstructure and Tribological Properties of FeCoNiCuAl High-Entropy Alloy Produced by Laser Powder Bed Fusion. *Virtual Phys. Prototyp.* **2020**, *15*, 543–554. [CrossRef]
16. Gokcekaya, O.; Hayashi, N.; Ishimoto, T.; Ueda, K.; Narushima, T.; Nakano, T. Crystallographic Orientation Control of Pure Chromium via Laser Powder Bed Fusion and Improved High Temperature Oxidation Resistance. *Addit. Manuf.* **2020**, *36*, 101624. [CrossRef]
17. Liu, X.; Wang, K.; Hu, P.; He, X.; Yan, B.; Zhao, X. Formability, Microstructure and Properties of Inconel 718 Superalloy Fabricated by Selective Laser Melting Additive Manufacture Technology. *Materials* **2021**, *14*, 991. [CrossRef]
18. Mukherjee, T.; Zuback, J.S.; De, A.; DebRoy, T. Printability of Alloys for Additive Manufacturing. *Sci. Rep.* **2016**, *6*, 19717. [CrossRef]
19. Oliveira, J.P.; LaLonde, A.D.; Ma, J. Processing Parameters in Laser Powder Bed Fusion Metal Additive Manufacturing. *Mater. Des.* **2020**, *193*, 108762. [CrossRef]

20. Giorgetti, A.; Baldi, N.; Palladino, M.; Ceccanti, F.; Arcidiacono, G.; Citti, P. A Method to Optimize Parameters Development in L-PBF Based on Single and Multitracks Analysis: A Case Study on Inconel 718 Alloy. *Metals* **2023**, *13*, 306. [CrossRef]
21. Johnson, L.; Mahmoudi, M.; Zhang, B.; Seede, R.; Huang, X.; Maier, J.T.; Maier, H.J.; Karaman, I.; Elwany, A.; Arróyave, R. Assessing Printability Maps in Additive Manufacturing of Metal Alloys. *Acta Mater.* **2019**, *176*, 199–210. [CrossRef]
22. Agarwal, N.; Monu, M.C.C.; Selvam, K.T.; Obeidi, M.A.; Brabazon, D. Study of the Effects of Laser Power and Scanning Speed on the Microstructural Morphologies and Physical Properties of L-PBF Produced Ni52.39Ti47.61. *J. Mater. Res. Technol.* **2023**, *27*, 8334–8343. [CrossRef]
23. Tenbrock, C.; Fischer, F.G.; Wissenbach, K.; Schleifenbaum, J.H.; Wagenblast, P.; Meiners, W.; Wagner, J. Influence of Keyhole and Conduction Mode Melting for Top-Hat Shaped Beam Profiles in Laser Powder Bed Fusion. *J. Mater. Process. Technol.* **2019**, *278*, 116514. [CrossRef]
24. King, W.E.; Barth, H.D.; Castillo, V.M.; Gallegos, G.F.; Gibbs, J.W.; Hahn, D.E.; Kamath, C.; Rubenchik, A.M. Observation of Keyhole-Mode Laser Melting in Laser Powder-Bed Fusion Additive Manufacturing. *J. Mater. Process. Technol.* **2014**, *214*, 2915–2925. [CrossRef]
25. Khorasani, M.; Ghasemi, A.; Leary, M.; Downing, D.; Gibson, I.; Sharabian, E.G.; Veetil, J.K.; Brandt, M.; Bateman, S.; Rolfe, B. Benchmark Models for Conduction and Keyhole Modes in Laser-Based Powder Bed Fusion of Inconel 718. *Opt. Laser Technol.* **2023**, *164*, 109509. [CrossRef]
26. Tian, Y.; Tomus, D.; Rometsch, P.; Wu, X. Influences of Processing Parameters on Surface Roughness of Hastelloy X Produced by Selective Laser Melting. *Addit. Manuf.* **2016**, *13*, 103–112. [CrossRef]
27. Ning, J.; Wang, W.; Zamorano, B.; Liang, S.Y. Analytical Modeling of Lack-of-Fusion Porosity in Metal Additive Manufacturing. *Appl. Phys. A* **2019**, *125*, 1–11. [CrossRef]
28. Mukherjee, T.; DebRoy, T. Mitigation of Lack of Fusion Defects in Powder Bed Fusion Additive Manufacturing. *J. Manuf. Process.* **2018**, *36*, 442–449. [CrossRef]
29. Makoana, N.W.; Yadroitsava, I.; Möller, H.; Yadroitsev, I. Characterization of 17-4PH Single Tracks Produced at Different Parametric Conditions towards Increased Productivity of LPBF Systems—The Effect of Laser Power and Spot Size Upscaling. *Metals* **2018**, *8*, 475. [CrossRef]
30. Manvatkar, V.; De, A.; DebRoy, T. Heat Transfer and Material Flow during Laser Assisted Multi-Layer Additive Manufacturing. *J. Appl. Phys.* **2014**, *116*, 124905. [CrossRef]
31. Liu, Z.; Yang, Y.; Wang, D.; Chen, J.; Xiao, Y.; Zhou, H.; Chen, Z.; Song, C. Flow Field Analysis for Multilaser Powder Bed Fusion and the Influence of Gas Flow Distribution on Parts Quality. *Rapid Prototyp. J.* **2022**, *28*, 1706–1716. [CrossRef]
32. Wen, P.; Qin, Y.; Chen, Y.; Voshage, M.; Jauer, L.; Poprawe, R.; Schleifenbaum, J.H. Laser Additive Manufacturing of Zn Porous Scaffolds: Shielding Gas Flow, Surface Quality and Densification. *J. Mater. Sci. Technol.* **2018**, *35*, 368–376. [CrossRef]
33. Wen, P.; Jauer, L.; Voshage, M.; Chen, Y.; Poprawe, R.; Schleifenbaum, J.H. Densification Behavior of Pure Zn Metal Parts Produced by Selective Laser Melting for Manufacturing Biodegradable Implants. *J. Mater. Process. Technol.* **2018**, *258*, 128–137. [CrossRef]
34. Zhang, W.; Guo, D.; Wang, L.; Davies, C.M.; Mirihanage, W.; Tong, M.; Harrison, N.M. X-Ray Diffraction Measurements and Computational Prediction of Residual Stress Mitigation Scanning Strategies in Powder Bed Fusion Additive Manufacturing. *Addit. Manuf.* **2022**, *61*, 103275. [CrossRef]
35. Huang, T.-C.; Hung, C.-H.; Lin, Y. Residual Stress Reduction in Ti-6Al-4V Parts Fabricated by Laser-Foil-Printing Process. *Opt. Laser Technol.* **2024**, *177*, 111157. [CrossRef]
36. Zhang, L.; Zhang, S.; Zhu, H. Effect of Scanning Strategy on Geometric Accuracy of the Circle Structure Fabricated by Selective Laser Melting. *J. Manuf. Process.* **2021**, *64*, 907–915. [CrossRef]
37. Marattukalam, J.J.; Karlsson, D.; Pacheco, V.; Beran, P.; Wiklund, U.; Jansson, U.; Hjörvarsson, B.; Sahlberg, M. The Effect of Laser Scanning Strategies on Texture, Mechanical Properties, and Site-Specific Grain Orientation in Selective Laser Melted 316L SS. *Mater. Des.* **2020**, *193*, 108852. [CrossRef]
38. Amano, H.; Ishimoto, T.; Suganuma, R.; Aiba, K.; Sun, S.-H.; Ozasa, R.; Nakano, T. Effect of a Helium Gas Atmosphere on the Mechanical Properties of Ti-6Al-4V Alloy Built with Laser Powder Bed Fusion: A Comparative Study with Argon Gas. *Addit. Manuf.* **2021**, *48*, 102444. [CrossRef]
39. Bidare, P.; Bitharas, I.; Ward, R.M.; Attallah, M.M.; Moore, A.J. Laser Powder Bed Fusion in High-Pressure Atmospheres. *Int. J. Adv. Manuf. Technol.* **2018**, *99*, 543–555. [CrossRef]
40. Reijonen, J.; Revuelta, A.; Riipinen, T.; Ruusuvuori, K.; Puukko, P. On the effect of shielding gas flow on porosity and melt pool geometry in laser powder bed fusion additive manufacturing. *Addit. Manuf.* **2020**, *32*, 101030. [CrossRef]
41. Pauzon, C.; Forêt, P.; Hryha, E.; Arunprasad, T.; Nyborg, L. Argon-Helium Mixtures as Laser-Powder Bed Fusion Atmospheres: Towards Increased Build Rate of Ti-6Al-4V. *J. Mater. Process. Technol.* **2019**, *279*, 116555. [CrossRef]
42. Childs, T.H.C.; Hauser, C.; Badrossamay, M. Mapping and Modelling Single Scan Track Formation in Direct Metal Selective Laser Melting. *CIRP Ann.* **2004**, *53*, 191–194. [CrossRef]

43. Guo, Y.; Jia, L.; Kong, B.; Wang, N.; Zhang, H. Single Track and Single Layer Formation in Selective Laser Melting of Niobium Solid Solution Alloy. *Chin. J. Aeronaut.* **2017**, *31*, 860–866. [CrossRef]
44. Shrestha, S.; Chou, K. Single Track Scanning Experiment in Laser Powder Bed Fusion Process. *Procedia Manuf.* **2018**, *26*, 857–864. [CrossRef]
45. Balbaa, M.; Mekhiel, S.; Elbestawi, M.; McIsaac, J. On Selective Laser Melting of Inconel 718: Densification, Surface Roughness, and Residual Stresses. *Mater. Des.* **2020**, *193*, 108818. [CrossRef]
46. Yadroitsava, I.; Els, J.; Booysen, G.; Yadroitsev, I. Peculiarities of single track formation from TI6AL4V alloy at different laser power densities by selective laser melting. *S. Afr. J. Ind. Eng.* **2015**, *26*, 86–95. [CrossRef]
47. Lerda, S.; Bassini, E.; Marchese, G.; Biamino, S.; Ugues, D. Rapid L-PBF Printing of IN718 Coupled with HIP-Quench: A Novel Approach to Manufacture and Heat Treatment of a Nickel-Based Alloy. *J. Mater. Res. Technol.* **2024**, *30*, 6983–6994. [CrossRef]
48. Watring, D.S.; Carter, K.C.; Crouse, D.; Raeymaekers, B.; Spear, A.D. Mechanisms Driving High-Cycle Fatigue Life of as-Built Inconel 718 Processed by Laser Powder Bed Fusion. *Mater. Sci. Eng. A* **2019**, *761*, 137993. [CrossRef]
49. Baldi, N.; Giorgetti, A.; Palladino, M.; Arcidiacono, G.; Citti, P. Thermal Design Considerations for a L-PBF Built Metal Component: Effects of Inter-Layer Cooling Time, Preheating Temperature and Gas Flow. *IOP Conf. Ser. Mater. Sci. Eng.* **2024**, *1306*, 012020. [CrossRef]
50. Baldi, N.; Giorgetti, A.; Palladino, M.; Giovannetti, I.; Arcidiacono, G.; Citti, P. Study on the Effect of Preheating Temperatures on Melt Pool Stability in Inconel 718 Components Processed by Laser Powder Bed Fusion. *Metals* **2023**, *13*, 1792. [CrossRef]
51. Kan, W.H.; Chiu, L.N.S.; Lim, C.V.S.; Zhu, Y.; Tian, Y.; Jiang, D.; Huang, A. A critical review on the effects of process-induced porosity on the mechanical properties of alloys fabricated by laser powder bed fusion. *J. Mater. Sci.* **2022**, *57*, 9818–9865.
52. Gasper, A.N.D.; Szost, B.; Wang, X.; Johns, D.; Sharma, S.; Clare, A.T.; Ashcroft, I.A. Spatter and Oxide Formation in Laser Powder Bed Fusion of Inconel 718. *Addit. Manuf.* **2018**, *24*, 446–456. [CrossRef]